Kinetic neoclassical calculations of impurity radiation profiles

D.P. Stotler [a,*], D.J. Battaglia [a], R. Hager [a], K. Kim [b], T. Koskela [c], G. Park [d], M.L. Reinke [e]

[a] *Princeton Plasma Physics Laboratory, Princeton University, P. O. Box 451, Princeton, NJ 08543-0451, USA*
[b] *KAIST, Daejeon, South Korea*
[c] *Lawrence Berkeley National Laboratory, Berkeley, CA 94720 USA*
[d] *National Fusion Research Institute, Daejeon, South Korea*
[e] *Oak Ridge National Laboratory, P. O. Box 2008, Oak Ridge, TN 37831, USA*

A B S T R A C T

Modifications of the drift-kinetic transport code XGC0 to include the transport, ionization, and recombination of individual charge states, as well as the associated radiation, are described. The code is first applied to a simulation of an NSTX H-mode discharge with carbon impurity to demonstrate the approach to coronal equilibrium. The effects of neoclassical phenomena on the radiated power profile are examined sequentially through the activation of individual physics modules in the code. Orbit squeezing and the neoclassical inward pinch result in increased radiation for temperatures above a few hundred eV and changes to the ratios of charge state emissions at a given electron temperature. Analogous simulations with a neon impurity yield qualitatively similar results.

1. Introduction

Extrapolation of empirical transport trends predicts that to maintain divertor heat loads at tolerable levels, ITER will need to radiate 80% of its total input power, with roughly 30% coming from the core [1]. The requirements for DEMO are more severe yet, with a total radiated fraction of $\sim$90% and $\sim$50% from the core [2]. An understanding of the spatial distribution of impurity radiation in the edge and scrape-off layer (SOL) of tokamaks is needed to ensure that such predictions are as accurate as possible. While existing diagnostics techniques, such as resistive bolometry, can determine the integrated amount of power radiated, they have very poor spatial resolution. The need for better spatial resolution is especially critical in the steep gradient region of the H-mode pedestal and near the X-point where shifts of a cm or a few mm can dramatically alter the division of the cooling between closed and open flux surfaces.

The bulk of the tokamak impurity transport and radiation modeling to date has been carried out via fluid plasma codes solving the Braginskii equations [3–5]. While these do provide spatially resolved, and time dependent profiles of the impurity charge state distributions and the associated radiation, they inherently miss the

kinetic and non-local neoclassical effects on ion transport that can be dominant [6,7] in the steep pedestal region of H-mode plasmas.

The full-f, drift-kinetic, multi-species, particle-in-cell (PIC) transport code XGC0 [8] has been applied previously to examine kinetic and non-local neoclassical effects on the main ion plasma [7,8], including self-consistently determined radial electric field and sheath potential to ensure ambipolarity, as well as neutral recycling and ionization [9]. An acknowledged limitation of the work reported in [7] is that the carbon impurity had a fixed charge (6+) and the associated radiative cooling was not consistently determined.

We describe here the extension of XGC0 to resolve the individual impurity charge states and to track the associated radiation and electron cooling/heating, taking another step towards a nearly first principles tool for fusion plasma simulation. Generalized collisional radiative (GCR) rates are used for all atomic physics processes [10,11]. Starting with input plasma profiles based on an NSTX H-mode discharge, the deuterium ion and impurity species are evolved in time towards neoclassical transport equilibrium, including a recycling source determined from consistent neutral deuterium and impurity density profiles. To facilitate comparison of the spatial distribution of the radiated power with that obtained from coronal equilibrium (CE), the electron density and temperature profiles are held fixed throughout.

Section 2 describes the implementation of impurity ionization and recombination into XGC0 and the associated assumptions.

* Corresponding author.
  E-mail address: dstotler@pppl.gov (D.P. Stotler).

That the resulting model is consistent with coronal equilibrium is demonstrated in Section 3. The effects of neoclassical phenomena on the impurity charge state distribution and radiation profile are detailed in Section 4. Finally, in Section 5, we summarize and discuss related work planned for the future.

2. Implementation of multiple charge states in XGC0

The XGC family of codes began with the five dimensional (three space, two velocity), full-f, drift-kinetic PIC code described in [8]. That code and all subsequent versions of XGC0 have at their core a particle pushing algorithm that integrates the Hamiltonian equations of motion [8,12] in time for a set of marker particles representing the ion (and electron, when included) guiding centers. The algorithm is designed to work efficiently and accurately in a magnetic separatrix geometry based on a numerically specified equilibrium, allowing plasma transport to be simulated from the magnetic axis to the material surfaces. A second critical component of XGC0 is the temporal evolution of the radial electric field via Ampere's law averaged over a closed flux surface [8]. The principal effect of the electric field is to increase the energy thresholds for X-loss [8,13,14] (small parallel velocity ions near the X-point that ∇B drift across the separatrix into the divertor) and orbit loss [14,15] enough that the associated sinks of energetic main ions can be offset by the inward pinch [16,17] of colder ions and impurities, maintaining ambipolar plasma transport across the separatrix.

XGC0 has many capabilities beyond these, some that will be utilized in this work, some that will not. The specific ones used here, and the relevant physical phenomena are:

- *Particle push:* introduces finite banana orbit width,
- *Radial electric field:* gives rise to orbit squeezing,
- *Recycling:* the impurity source replacing X- and orbit-, and transport losses,
- *Fokker-Planck collisions:* produce pitch angle scattering, inward pinch, and other neoclassical effects.

Improvements to XGC0 since the original version that we do *not* use in this work are: diffusive anomalous transport, logical sheath (provides a constant plasma potential in SOL) [7] and three-dimensional magnetic perturbations [18].

The variety of problems that can be studied with XGC0 has been limited by the fixed charge state of the impurity species and the relatively simple models available for describing impurity radiation [19,20]. We relax these limitations by including the particle charge state as an additional phase space parameter that can vary in time; the code modifications required with this approach are simpler than those associated with treating each charge state as a distinct particle "species". For low-Z elements, such as carbon or neon, all charge states can be readily included in the simulations. Treating high-Z species, e.g., molybdenum or tungsten, will likely require the use of "bundled" representations of the atom's electronic structure [21]. Our implementation allows for this possibility by specifying the charge states associated with each impurity species with an array of arbitrary length.

The temporal evolution of the particle charge states via electron impact ionization and recombination is effected by a Monte Carlo algorithm directly analogous to that used in simulating the ionization of neutral particles [8,9]. Generalized collisional radiative rates (metastable unresolved) for these processes, as well as the associated electron cooling and heating rates, have been extracted from the ADAS database [10] and made accessible to XGC0 via a new interface to the DEGAS 2 neutral transport code [22] developed expressly for this purpose. Since the electron density and temperature profiles are held fixed in the present work, we defer to a future publication a description of our approach to incorpo-

rating the effects of ionization and recombination on the electron population.

Note that XGC0, like most transport codes, works internally with the rate at which electrons lose or gain energy as impurities are being ionized and recombined. To show how this relates to the more experimentally relevant radiated power, we first write the equivalent expression for the local time rate of change of the density of impurity charge state q, ignoring collisions, transport, etc.:

$$\frac{\partial n_q}{\partial t} = -n_q n_e S_q + n_{q+1} n_e R_{q+1} + n_{q-1} n_e S_{q-1} - n_q n_e R_q + Q_q, \qquad (1)$$

with $q = 1 \to Z$; S_0 is the rate at which neutral impurities are ionized, and $R_{Z+1} = S_Z = 0$. The S_q and R_q are the GCR rates, "SCD" and "ACD" in ADAS nomenclature, respectively. The "source" term Q_q represents the sinks due to X-, orbit-, and transport losses. The corresponding equations for neutral species is

$$n_0 n_e S_0 = n_1 n_e R_1 + Q_0, \qquad (2)$$

since the neutral transport model assumes steady state; Q_0 represents the recycling source.

In terms of these quantities, the electron cooling power associated with charge state q is then

$$P_{\text{cool},q} = E_{\text{ion},q}(n_q n_e S_q - n_{q+1} n_e R_{q+1}) + n_q n_e P_{\text{ion},q} + n_{q+1} n_e P_{\text{rec},q+1}, \qquad (3)$$

where $q = 1 \to Z - 1$ (losses associated with neutral ionization are not tallied here; these will be estimated), and $E_{\text{ion}, q}$ is the energy required to ionize the $+q$ ion. $P_{\text{ion}, q}$ ("PLT" in ADAS) and $P_{\text{rec},q+1}$ ("PRB') are the total rates of line emission associated with ionization and recombination, respectively, between charge states q and $q + 1$. Eq. (3) is equivalent to Eq. (27) of [11], although demonstrating the correspondence requires some manipulation of terms. The corresponding expression for the radiated power is:

$$P_{\text{rad},q} = n_q n_e P_{\text{ion},q} + n_{q+1} n_e P_{\text{rec},q+1}. \qquad (4)$$

In CE, $n_q/n_{q+1} = R_{q+1}/S_q \Rightarrow P_{\text{cool},q} = P_{\text{rad},q}$. Away from CE, e.g., if $\partial n_q/\partial t \neq 0$ and / or $Q_q \neq 0$, this may not be true. Apart from the earliest time steps of the run described in Section 3, all of the data have $\partial n_q/\partial t$ and Q_q small enough that the two quantities are qualitatively similar. Consequently, we treat the terms "electron cooling" and "radiated power" as interchangeable. Namely, the plots below actually depict the electron cooling compiled by the code, but we will refer to it as the radiated power.

Related quantities include the total impurity density, $n_I = \sum_{q=1}^{Z} n_q$, total "radiated" power:

$$P_{\text{rad}} \equiv \sum_{q=1}^{Z-1} P_{\text{cool},q}, \qquad (5)$$

and, as in [23–25], the effective "radiated" power per electron and impurity ion:

$$L_{\text{rad}} \equiv P_{\text{cool}}/(n_e n_I). \qquad (6)$$

The electron densities and temperatures required to evaluate the GCR rates are compiled on a 2-D mesh that, on closed flux surfaces, coincides with that used by the linear Fokker-Planck collision operator. For all simulations described here, this mesh (Fig. 1) consists of 50 cells spaced uniformly in poloidal flux between $\psi_n \equiv \psi/\psi_{\text{sep}} = 0.4$ and the separatrix, and four divisions uniform in poloidal angle, with the first centered about the outboard midplane. The SOL regions above and below the X-point are represented by five cells each, up to $\psi_n = 1.05$. The entirety of the lower private flux region (PFR) is incorporated into one additional cell. All relevant output data are compiled on this same mesh, although the results shown here have been reduced to one dimension by
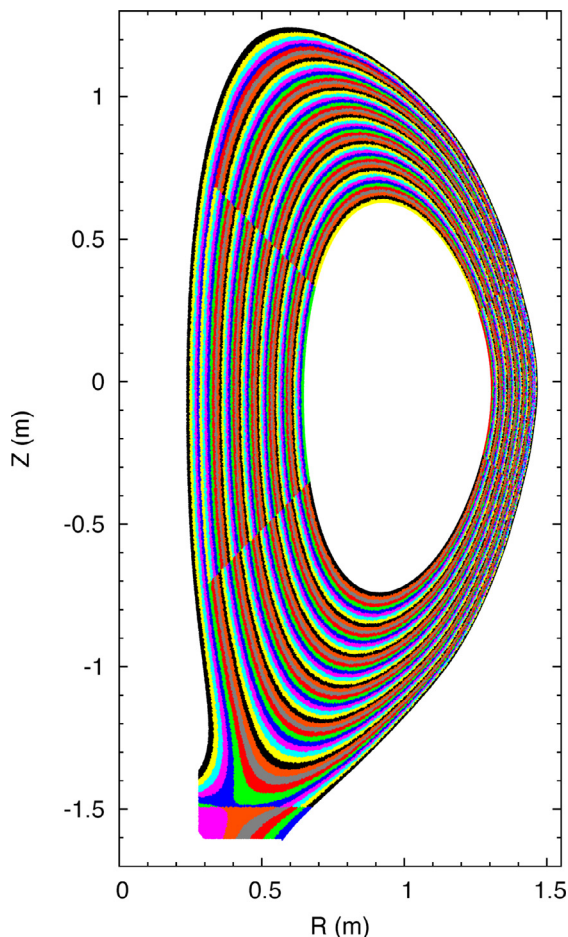
Fig. 1. Mesh used for compiling the electron densities and temperatures required to evaluate the GCR rates, as well as for the output data. The closed flux surface portion of the mesh is also used by the Fokker–Planck collision operator. The colors depicted have been chosen solely to allow the mesh cells to be distinguished and do not represent any physical quantity.

poloidal averaging. As with previous XGC0 applications [7,9,26], our emphasis will be on phenomena in the confined plasma, with relatively simple models of open field line behavior to facilitate the specification of boundary conditions. More detailed treatment of SOL and PFR physics awaits the development of similar impurity transport capabilities in the XGCa code [27,28].

The source of impurity ions in previous XGC0 versions was assumed proportional to the source of (main) deuterium ions arising from the ionization of the atoms generated by recycling [7]. The neutral density profile used for this purpose is the result of a separate kinetic, Monte Carlo calculation performed on a fluid plasma background. The spatial variation of the neutral source for that process is taken to be proportional to flux of ions lost to the walls and divertor. Here, we extend this model by compiling separate neutral atom density profiles for each impurity species and then use them to determine the $1+$ ion particle source via the ADAS neutral ionization rate and the same Monte Carlo collision algorithm used for deuterium.

Presently, the poloidal distribution of the impurity neutral source is equal to that of the deuterium neutrals. As in the deuterium neutral transport model, the neutral source for all impurity species is characterized by a specified recycling rate, 99% here, and a 3 eV thermal energy distribution. These assumptions have been made in the interest of simplicity. We do expect the results to be sensitive to those particular values since the recycling coefficient determines the magnitude of the neutral source and since the

penetration depth scales with the square root of the birth energy. Only ionization (no charge exchange) is considered in the interactions of the neutral impurity atoms with the plasma. DEGAS 2 will ultimately be used to provide a more realistic characterization of the impurity source, e.g., via sputtering and neutral-plasma interactions, as well as recombination from the singly charged state.

XGC0 impurity simulations utilize a linear Fokker–Planck collision operator that explicitly conserves mass, momentum, and energy. The outermost loop of the collision operation is over species; each serves as a "background" for a standard Monte Carlo collision operation [29] for all other "test" species, including self-collisions. To generalize the procedure for multiple charge states, inner loops over charge states have been added to both loops over "background" and "test" species. The energy and momentum exchanged in the Monte Carlo collisions is tabulated as a function of space, as well as the "test" species and charge state. In the second stage of the linearized collision process, the "restoring" force of the Monte Carlo collisions on the background particles is applied using expressions in [30]. A third stage enforces particle, momentum, and energy conservation via a technique similar to that of [31].

If the density of a particular "background" charge state is zero in a mesh cell or if there are too few particles (< 100) to accurately compute a temperature, the collision operations in that cell are bypassed completely for that charge state. Additional numerical difficulties may arise for low, but non-zero, background density states. As a first step towards their mitigation, the global energy exchange in the Monte Carlo collisions is summed over test species and compared with the corresponding sum for the D^+ background. If the ratio is $< 1\%$, the second and third stages of the collision routine are bypassed. In practice, the routine is not entirely robust, and its conservation properties are poorer than its operation with fixed charge state impurities. The resulting error in a simulation is quantified below. Continued refinements in the model and its verification via conservation and equilibration tests [27] will be discussed in a subsequent publication.

3. Approach to coronal equilibrium

To verify the ionization-recombination model and to provide a starting point for quantifying the effects of neoclassical phenomena, we demonstrate the approach to coronal equilibrium starting from singly charged carbon ions. Note that the code possesses no method for initializing the simulation with only neutral impurity atoms. To make contact with standard references on the topic, e.g., [23–25], we disable all physical processes in the code apart from ionization and recombination; the simulation particles are *not* moving. The particular ADAS files used are from the "96" set and are dated November 4, 1999.

The magnetic equilibrium input to XGC0 is from the NSTX ELMy H-mode shot 139047 at 580 ms. The electron and carbon density and temperature profiles in Fig. 2 are similar to those obtained from the diagnostic output from this shot during the last half of the ELM cycle, as depicted and analyzed in [32]; note, though, that no initial toroidal rotation is specified for our simulations. Again, the electron density and temperature profiles are held fixed to allow the effects of neoclassical phenomena on the impurity ions to be elucidated. A deuterium density profile is computed from the electron and carbon density profiles via quasi-neutrality; the input deuterium temperature is assumed to the same as that of carbon. The initial particle positions, velocities, and weights for both ion species are sampled from their respective profiles [7]. The deuterium and carbon moments are computed and output periodically as the simulation evolves in time.

This simulation is run in three parts, with the time step increasing a factor of ten with each restart; the total time elapsed is 22 ms. The L_{rad} values are computed as integrals over each ra-
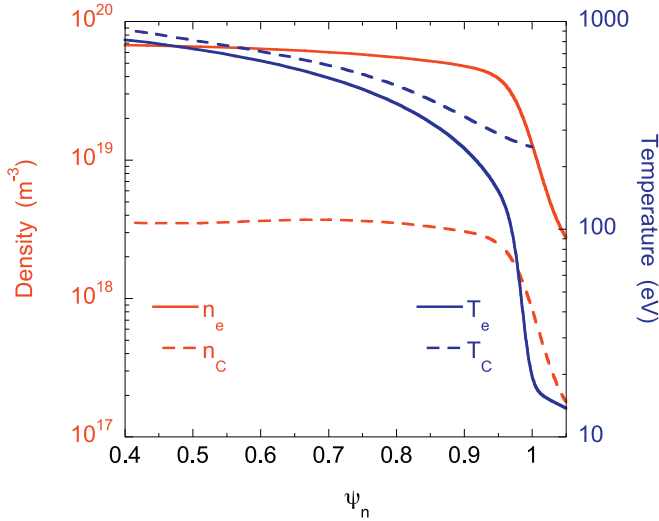
Fig. 2. The temperature (right axis) and density (left axis) profiles for electrons (solid curves) and carbon (initial; dashed curves) input to XGC0 are based on NSTX ELMy H-mode discharge 139047 at 580 ms [32]. The initial deuterium density is computed via quasi-neutrality. The electron profiles are held fixed while all others evolve in time.

dial zone and then plotted as a function of the average T_e in that zone (Fig. 3(a)); the curves are labeled by the total elapsed time. This situation is not directly analogous to those in [23,24] since n_e varies with T_e across our simulation's radial profile. Nonetheless, the simulated curves converge towards the CE, computed directly from the ADAS rates, at roughly the same pace as in [24]. The final charge state distribution, Fig. 3(b), also compares well with that of CE.

4. Neoclassical effects on radiation profile

The simulations discussed in this section either begin with the near-equilibrium state obtained above or with a CE charge state distribution computed directly from the ADAS rates; the results of the two approaches are similar.

We first enable the ion particle push to assess the effect of orbit width on L_{rad}. Carbon ion orbits in the steep gradient region have widths on the order of $\Delta\psi/\psi_{sep} = 0.02$, comparable to the

electron density and temperature gradient scale lengths. These orbit widths are reduced by the "orbit squeezing" [8] associated with the radial electric field.

The effect of non-zero orbit width is incorporated into the initial coronal equilibrium since the ion starting positions are sampled at all points along the orbits. The orbital periods in the steep gradient region are on the order of 10^{-4} s, much shorter than the relevant recombination ($\sim 10^{-2}$ s) and ionization ($>10^{-3}$ s) times. Consequently, the variations in density and temperature average out to some degree, and we would not expect the charge state distribution to deviate significantly from CE.

The initial state of this simulation has no electric field so that orbit squeezing does not take effect until the radial electric field has been established. This squeezing not only reduces the orbit widths, but also rapidly shifts them inward, on average, to higher n_e, T_e surfaces and, thus, pushes them out of CE. The relative increases in the C^{4+} and C^{5+} fractions result in enhanced L_{rad} around $T_e \simeq 200$ eV ($\psi_n \simeq 0.93$) early in the simulation ($t = 1.4 \times 10^{-4}$ s; dashed blue curve in Fig. 4(a)). The charge state distribution eventually adjusts to the shift, and the effective L_{rad} decays towards the CE result ($t = 4.6 \times 10^{-3}$ s; solid blue curve).

We next incorporate a source of impurities, the aforementioned 99% recycling rate that replaces the ions lost to the walls by X-, orbit-, and transport loss. The initial impact of the resulting influx of low charge state ions [dashed green curve in Fig. 4(a)] is large, with significant increases in L_{rad} for $T_e < 200$ eV. However, the recycled ions are too low in energy to enter the loss cone so that this effect also decays for $T_e \geq 30$ eV, and L_{rad} again approaches the CE value (solid green curve). The elevated values below 30 eV represent ongoing recycling in the SOL.

The inclusion of collisions via the linearized Fokker–Planck operator introduces pitch angle scattering of the carbon ions off of deuterium and other carbon ions, moving some ions from confined to loss orbits and resulting in a nearly steady state enhancement of the radiation at lower electron temperatures (orange curves in Fig. 4(a)). Note that anomalous transport, which will be included in discharge-specific simulations (as in [7]), provides another mechanism for moving ions onto loss orbits. By the later time, the neoclassical inward pinch has boosted the population of C^{4+} and C^{5+} in the core region of the simulation, increasing the effective L_{rad} for $T_e > 250$ eV (solid orange curve in Fig. 4(a)). That the inward pinch now carries a non-trivial distribution of carbon charge states represents an improvement in the determination of the radial ion
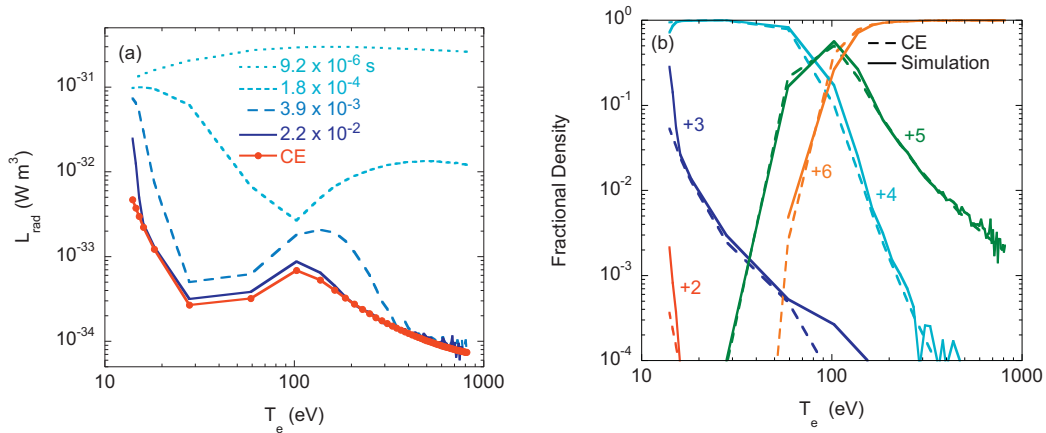
Fig. 3. (a) Radiation rates per carbon ion and per electron integrated over each radial zone in the simulation and plotted as a function of the average electron temperature in that zone, resulting in curves analogous to those in [23–25]. The "CE" curve is computed directly from the ADAS rates evaluated at each T_e, n_e in the simulation. The blue curves represent different times during the run. Note that the lowest (highest) T_e, the outermost (core boundary) surface, corresponds to a density $n_e = 3.1 \times 10^{18}$ m^{-3} (6.8 $\times 10^{19}$ m^{-3}). (b) The final ($t = 22$ ms) fractional charge state densities (solid) are compared with the corresponding CE values (dashed). In the simulation, $n_1/n_I = 0$; for CE, $n_1/n_I < 10^{-7}$. (For interpretation of the references to colour in this figure legend, the reader is referred to the web version of this article.)
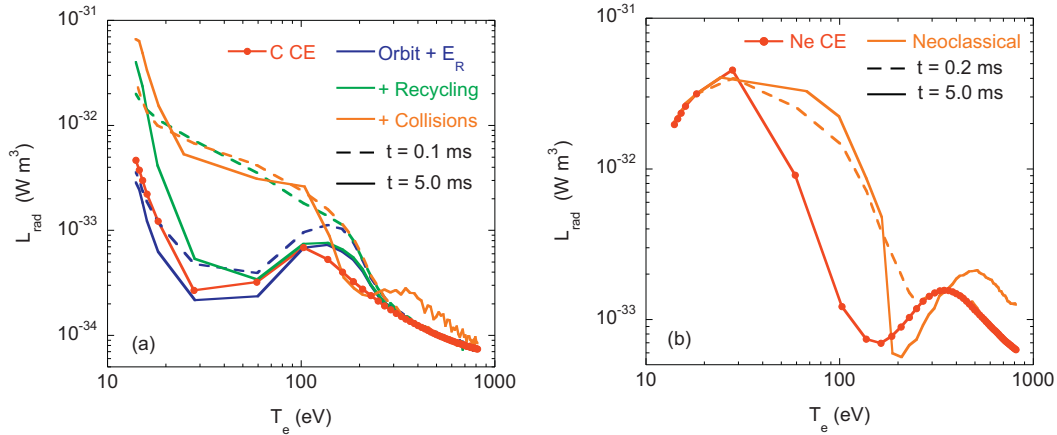
Fig. 4. In (a), neoclassical phenomena are added to the simulations in steps, with L_{rad} curves shown for each step at an early time, $t = 0.1$ ms (dashed), and at a later time, $t = 5.0$ ms (solid). All are initialized with a coronal equilibrium charge state distribution. Each of these runs can be compared with the coronal equilibrium result (red), as in Fig. 3. In the first simulation (blue), the particle push is enabled and self-consistent radial electric field is computed. The result of then adding neutral recycling for both deuterium and carbon is depicted by the green curves. Finally, including collisions results in the orange curves. (b) An analogous simulation with all processes in effect is run with a neon impurity, yielding the orange curves, shown at $t = 0.2$ ms (dashed) and 0.5 ms (solid). The corresponding coronal value is shown in red. (For interpretation of the references to colour in this figure legend, the reader is referred to the web version of this article.)
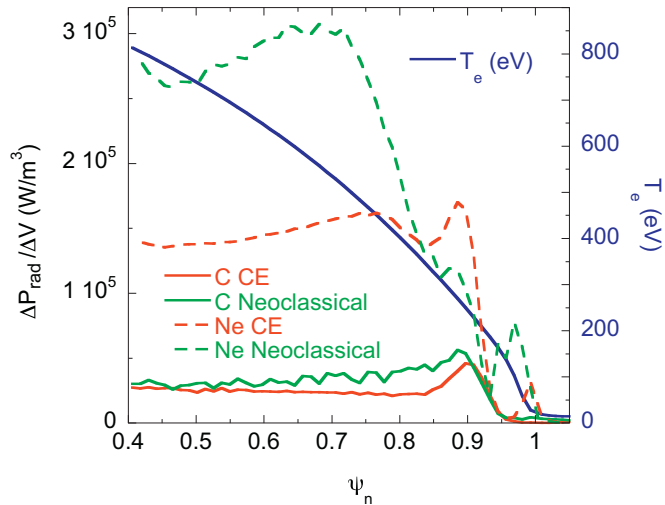
Fig. 5. Radial profiles of the integrated radiation density as function of the normalized poloidal flux for the equilibrium (red) and neoclassical (green) cases in the runs with carbon (solid) and neon (dashed) impurity. These profiles represent the contribution to the total radiation made by each radial cell in the mesh (ΔP) divided by its volume (ΔV). The T_e profile (blue) from Fig. 2 is included for reference. (For interpretation of the references to colour in this figure legend, the reader is referred to the web version of this article.)

Fig. 6. Relative contributions to the radiated power associated with ionization and recombination between the indicated carbon charge states at a given radial flux surface as a function of T_e there. The dashed curves ("CE") represent the equilibrium state shown in Fig. 3. The solid curves ("Neoclassical") are based on $t = 5$ ms in the "full physics" simulation. The maximum value of the fractional power from the $1 \leftrightarrow 2$ ($2 \leftrightarrow 3$) CE system is 3.8×10^{-6} (7.9×10^{-3}); these curves are not shown.

current and thus in the radial electric field calculation relative to that of previous XGC0 versions.

The numerical problems with the Fokker–Planck collision routine referred to in Section 2 result in a 2% gain in the total carbon population over the 50,000 steps of the simulation, a deviation too small to impact our conclusions. An analogous simulation with fixed ($+6$) charge state carbon ions yields essentially the same final density, flow velocity, and temperature profiles.

Incorporating neoclassical phenomena into the simulation results in a 36% increase in the radiated power relative over that of CE (0.24 MW and 0.18 MW, respectively). The bulk of this change arises for $\psi_n < 0.9$ even though the enhancements in L_{rad} are greater at lower temperatures simply because the densities are much lower outside the pedestal, as can be seen in a plot of the radiation density, $n_e n_C L_{rad}$, in Fig. 5. This figure depicts the same trend as in Fig. 4(a), but reflects the weighting by the densities.

The radiated power profile broken down by charge state as in Eq. (3) is compared with the CE result in Fig. 6. The neoclassical effects result in inward shifts of the contributions from $3 \leftrightarrow 4$ on up. Note that on this scale, the CE $1 \leftrightarrow 2$ and $2 \leftrightarrow 3$ components are essentially zero and are not shown. In the non-equilibrium simulation, X- and orbit loss and the compensating recycling source cause them to no longer be negligible. We estimate the losses associated with neutral ionization to be only ~ 50 W in this simulation. The absolute power associated with each charge state at a given T_e is only quantitatively different in the two situations. However, the *ratios* of the powers in two charge states, more readily measured spectroscopically, change dramatically. This result provides an effective basis for identifying the presence of these phenomena in experimental data.
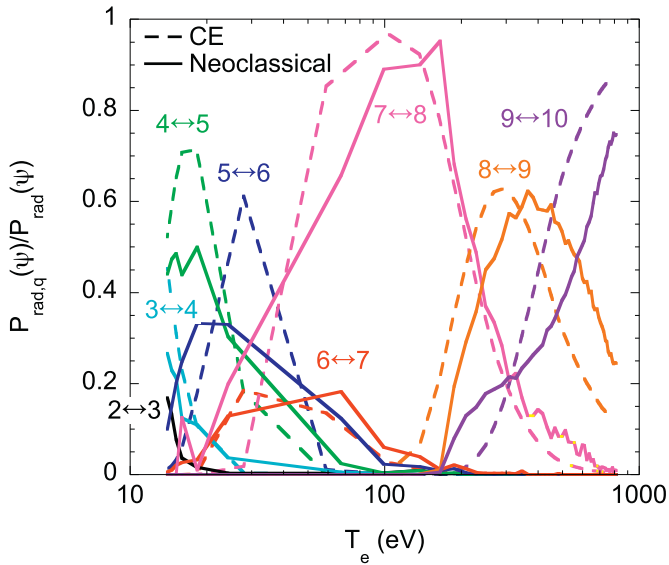
Fig. 7. Relative contributions to the radiated power associated with ionization and recombination between the indicated neon charge state at a given radial flux surface as a function of T_e there. The dashed curves ("CE") represent the equilibrium state. The solid curves ("Neoclassical") are based on $t = 5$ ms in the "full physics" simulation. The maximum value of the fractional power radiated by the $1\leftrightarrow2$ system is 2.7×10^{-5} for CE and 0.020 for the neoclassical run. For the $2\leftrightarrow3$ CE system, the maximum fractional radiated power is 1.4×10^{-2}. These three systems are not shown in the plot.

We have performed an analogous simulation with neon impurity for comparison. The initial density was set to half of the carbon density in Fig. 2, and an initial CE charge state distribution was used. The ADAS "96" files were dated June 11, 2014. As with carbon, the effective $L_{\rm rad}$ diverges from CE very early in the simulation, but not for $T_e < 30$ eV or $T_e > 300$ eV ($t = 0.2$ ms; dashed orange curve in Fig. 4(b)). As the calculation progresses, and the neon ions are pinched in, $L_{\rm rad}$ is enhanced by almost a factor of two in the core of the simulation. Again due to the weighting by the densities, this increase carries over into the total radiated power, which is 65% larger than the CE value (1.58 MW vs. 0.95 MW), and into the radiation density, Fig. 5. The shifts in the individual charge state contributions, Fig. 7 are reminiscent of those seen for carbon. The losses due to neutral neon ionization are estimated to be ~10 W, again negligibly small.

5. Conclusions

We have described the incorporation of impurity ionization and recombination into the drift-kinetic transport code XGC0. We ran this code with an NSTX H-mode plasma to illustrate the effects of neoclassical phenomena, including orbit squeezing, ion X- and orbit loss, neutral recycling, and inward pinch, on the impurity charge state distributions and radiation profile. The principal result for a carbon impurity is an increase in the effective radiation per electron and ion, $L_{\rm rad}$, for virtually all electron temperatures in the simulated plasma. The enhancement for $T_e > 250$ eV associated with the inward pinch acting on C^{4+} and C^{5+} ions results in a 36% increase in total radiated power relative to the value obtained with a coronal equilibrium charge state distribution. The ratios of the power radiated by two charge states at a given electron

temperature are even more strongly impacted by these effects. An analogous simulation with neon impurity yields qualitatively similar effects.

XGC0 simulations including kinetic electrons, and the effects of impurity radiation on their energy balance, are currently underway and will be reported in a future publication. The inclusion of diffusive anomalous transport and core particle, momentum, and energy sources will permit detailed modeling of individual experimental discharges, as in [7]. The next principal improvement to the model is the replacement of the XGC0 neutral transport model with DEGAS 2, a straightforward extension of the method described in [9]. This will provide improved spatial resolution along flux surfaces, allow the incorporation of other atomic physics processes, e.g., charge exchange of carbon ions with neutral hydrogen, and permit the use of more realistic plasma-material interactions and sputtering sources.

Acknowledgments

References

[1] A. Loarte, et al., Phys. Plasmas 18 (2011) 056105.
[2] R.P. Wenninger, et al., Nucl. Fusion 54 (2014) 114003.
[3] M. Groth, et al., J. Nucl. Mater. 415 (2011) S530.
[4] M. Wischmeier, et al., J. Nucl. Mater. 415 (2011) S523.
[5] C. Guillemaut, et al., J. Nucl. Mater. 438 (2013) S638.
[6] C.G. Wrench, et al., in: 38th EPS Conference on Plasma Physics 2011, EPS 2011 - Europhysics Conference Abstrats, 35, Strasbourg, France, 2011, pp. 1800–1802. 38th EPS Conference on Plasma Physics 2011, EPS 2011, 27 June - 1 July 2011
[7] D.J. Battaglia, et al., Phys. Plasmas 21 (2014) 072508.
[8] C.S. Chang, et al., Phys. Plasmas 11 (2004) 2649.
[9] D.P. Stotler, et al., Comput. Sci. Disc. 6 (2013) 015006.
[10] H.P. Summers, The ADAS User Manual, Version 2.6, 2002. http://www.adas.ac.uk
[11] H.P. Summers, et al., Plasma Phys. Control. Fusion 48 (2006) 263.
[12] M.F. Adams, et al., J. Phys. Conf. Ser. 180 (2009) 012036.
[13] C.S. Chang, et al., Phys. Plasmas 9 (2002) 3884.
[14] W.M. Stacey, Phys. Plasmas 18 (2011) 102504.
[15] K.C. Shaing, et al., Phys. Rev. Lett. 63 (1989) 2369.
[16] F.L. Hinton, R.D. Hazeltine, Rev. Mod. Phys. 48 (1976) 239.
[17] P. Helander, D.J. Sigmar, Collisional Transport in Magnetized Plasmas, Cambridge University Press, 2002. New York
[18] G. Park, et al., Phys. Plasmas 17 (2010) 102503.
[19] D.E. Post, et al., At. Data Nucl. Data Tables 20 (1977) 397.
[20] R.A. Hulse, Nucl. Tech. Fusion 3 (1983) 259.
[21] X. Bonnin, D. Coster, J. Nucl. Mater. 415 (2011) S488.
[22] D.P. Stotler, C.F.F. Karney, Contrib. Plasma Phys. 34 (1994) 392.
[23] P.G. Carolan, V.A. Piotrowicz, Plasma Phys. 25 (1983) 1065.
[24] D.E. Post, J. Nucl. Mater. 143 (1995) 220–222.
[25] A. Kallenbach, et al., Plasma Phys. Control. Fusion 55 (2013) 124041.
[26] D.P. Stotler, et al., J. Nucl. Mater. 438 (2013) S1275.
[27] R. Hager, et al., Phys. Plasma 23 (2016) 042503.
[28] R.M. Churchill, et al., Nucl. Mater. Energy. 2016, (these proceedings).
[29] A.H. Boozer, G. Kuo-Petravic, Phys. Fluids 24 (1981) 851.
[30] S.P. Hirshman, D.J. Sigmar, Phys. Fluids 19 (1976) 1532.
[31] W.X. Wang, et al., Plasma Phys. Control. Fusion 41 (1999) 1091.
[32] A. Diallo, et al., Nucl. Fusion 53 (2013) 093026.